



## Construction of 2D g-C<sub>3</sub>N<sub>4</sub>/MoS<sub>2</sub> heterojunction photocatalyst for enhanced degradation of pollution under visible light

Zijun Zhong, Ruopeng Xu, Huijuan He, Qiuna Zhuang, Langhuan Huang\*

Department of Chemistry, Jinan University, No. 601, The West of Huangpu Street, Guangzhou 510632, P.R. China, Tel. +862085223670; emails: [thuangleh@jnu.edu.cn](mailto:thuangleh@jnu.edu.cn) (L. Huang), [617997609@qq.com](mailto:617997609@qq.com) (Z. Zhong), [289281737@qq.com](mailto:289281737@qq.com) (R. Xu), [1138373032@qq.com](mailto:1138373032@qq.com) (H. He), [2457518220@qq.com](mailto:2457518220@qq.com) (Q. Zhuang)

Received 16 November 2017; Accepted 17 September 2018

### ABSTRACT

A novel g-C<sub>3</sub>N<sub>4</sub>/MoS<sub>2</sub> heterojunction photocatalyst with high efficient visible-light-region was fabricated by a facile calcination method. The composite with various weight ratios of g-C<sub>3</sub>N<sub>4</sub> and MoS<sub>2</sub> was synthesized and characterized. The results showed that MoS<sub>2</sub> was uniformly distributed on the surface of g-C<sub>3</sub>N<sub>4</sub>, resulting in the formation of heterostructure. The photocatalyst showed excellent photocatalytic activity in the photodegradation of organic pollutants. The optimized g-C<sub>3</sub>N<sub>4</sub>/MoS<sub>2</sub> sample (10-CN/M) exhibited 94% (Methylene Blue) degradation efficiency after being irradiated for 2 h under visible light. At last, the possible mechanism of the enhanced photocatalytic activity was discussed.

**Keywords:** Carbon nitride; Molybdenum sulfide; Photocatalysis; Visible light

### 1. Introduction

The photocatalytic technology has attracted much attention because of its potential as one of the strategies to solve the global energy and environmental issues [1,2]. To develop the photocatalytic technology with high efficiency, a great number of visible light-driven semiconductors have been designed, such as metal oxides, sulfides, and oxynitride. However, the high recombination rate of charge carriers, low usage of visible light, and poor catalytic activities have restricted its industrial application. Therefore, exploiting the high-efficiency, low-cost, and recyclable photocatalyst is the key to advance this technology into scalable commercial applications [3].

Recently, a metal-free photocatalyst, polymeric graphitic carbon nitride (g-C<sub>3</sub>N<sub>4</sub>) with high thermal and chemical stability, has attracted considerable attention for contaminant removal and hydrogen production from water splitting under visible light irradiation [4–8]. With the narrow

optical band gap (2.7 eV); the CB level is relatively negative, facilitating the reduction ability of the photogenerated electrons. In addition, with the strong covalent bonds between carbon and nitride atoms, g-C<sub>3</sub>N<sub>4</sub> is stable under light irradiation in solution with pH = 0–14 [9]. However, the several drawbacks of g-C<sub>3</sub>N<sub>4</sub>, such as low specific surface area, high recombination rate of photogenerated electron-hole pairs and low visible light utilization efficiency, consequently cannot satisfy the actual requirement [10,11]. To overcome these problems and improve the photocatalytic activity of g-C<sub>3</sub>N<sub>4</sub>, various strategies have been proposed, including doping and coupling with other materials to decrease the recombination rate of electron-hole pairs, morphology control to increase the surface area, chemical modification to enlarge the visible light absorption [12,13]. Among these efforts, coupling g-C<sub>3</sub>N<sub>4</sub> with other semiconductor photocatalysts to form the heterojunction (TiO<sub>2</sub>/g-C<sub>3</sub>N<sub>4</sub>, CdS/g-C<sub>3</sub>N<sub>4</sub>, ZnO/g-C<sub>3</sub>N<sub>4</sub>, and Bi<sub>2</sub>WO<sub>6</sub>/g-C<sub>3</sub>N<sub>4</sub>, etc.) has been proved to be efficient for the photodegradation of pollutants [14–17].

As one member of the emerging class of ultrathin two-dimensional (2D) transition-metal dichalcogenide (TMD)

\* Corresponding author.

nanomaterials, MoS<sub>2</sub> has attracted increasing research interest due to its unique structure and fascinating properties [18]. Moreover, MoS<sub>2</sub> has an intrinsic layered structure by stacking covalent bond S-Mo-S. Specifically, bulk MoS<sub>2</sub> is a band gap of about 1.3 eV, while the isolated MoS<sub>2</sub> monolayer possesses a large band gap of 1.8–1.9 eV because of quantum confinement effects [19]. Thus, it is suitable to couple with g-C<sub>3</sub>N<sub>4</sub> nanosheets to construct 2D/2D heterojunction owing to their suitable band gap and position of valence and conduction band. However, the 2D g-C<sub>3</sub>N<sub>4</sub>/MoS<sub>2</sub> heterojunctions with enhanced photocatalytic activity of photocatalytic degradation of organic dyes have been rarely reported.

Herein, the g-C<sub>3</sub>N<sub>4</sub>/MoS<sub>2</sub> (CNM) heterojunction photocatalysts were prepared by a facile calcination method. The activities of as-prepared photocatalyst were evaluated by the degradation of methylene blue (MB) under visible light illumination (>420 nm). The results indicated that g-C<sub>3</sub>N<sub>4</sub>/MoS<sub>2</sub> heterojunction photocatalyst exhibited enhanced photocatalytic activity compared with pure MoS<sub>2</sub> and pure g-C<sub>3</sub>N<sub>4</sub>. At the end of this work, a possible enhancement mechanism for the enhanced photocatalytic activity of g-C<sub>3</sub>N<sub>4</sub>/MoS<sub>2</sub> layered heterojunctions was also proposed.

## 2. Experimental

### 2.1. Materials

Sodium molybdate dihydrate (Na<sub>2</sub>MoO<sub>4</sub>·2H<sub>2</sub>O), thiourea, ethyl alcohol were purchased from Damao Chemical Reagent Co., Ltd (Tianjin, China). Melamine (99%) was purchased from Aladdin Chemistry Co., Ltd. (Shanghai, China). All materials were of analytical grade and used without any further purification. All aqueous solutions were prepared with ultrapure water (> 18 MΩ) from a Milli-Q Plus system (Millipore).

### 2.2. Preparation of MoS<sub>2</sub>

Pure MoS<sub>2</sub> was prepared from sodium molybdate dihydrate and thiourea. Briefly, sodium molybdate dihydrate and thiourea were mixed and grinded. The weight ratio of dihydrate/thiourea was fixed at 1:2. Then, the mixture was transferred in an alumina crucible with a cover. The alumina crucible was heated at 700°C for 2 h with a heating rate of

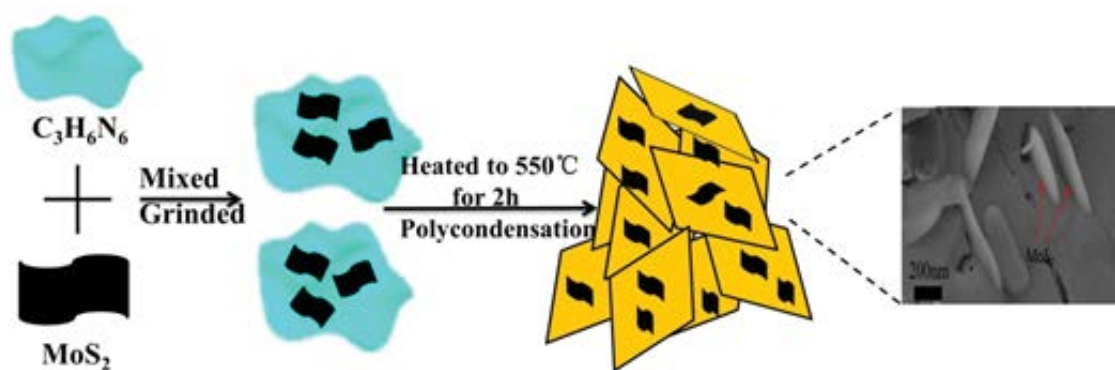
5°C/min in muffle furnace in a closed system. After natural cooling to room temperature, the resulting dark products were washed using ethanol and deionized water several times to remove the chemical residuals. Eventually, the products were obtained by drying at 60°C for 10 h in air and milled into powder for further use.

### 2.3. Preparation of CNM

The 2D g-C<sub>3</sub>N<sub>4</sub>/MoS<sub>2</sub> heterojunction was synthesized by a facile calcinations method. As shown in Scheme 1, pure MoS<sub>2</sub> and melamine were mixed and grinded. Then the mixture was transferred in an alumina crucible with a cover heated to 550°C at a heating rate of 5°C/min in tube furnace with flowing N<sub>2</sub> system and maintained for 2 h. After natural cooling to room temperature, the resulting dark green products were washed using ethanol and deionized water several times to remove the chemical residuals. Eventually, the powders were obtained by drying at 60°C for 10 h. The hybrid was denoted as 10-CNМ indicating that the weight ratio of melamine/pure MoS<sub>2</sub> was 10 in the hybrid. Moreover, pure g-C<sub>3</sub>N<sub>4</sub> was prepared by using melamine and industrial silicon dioxide as raw materials according to the method presented by Zhang and his colleagues [20].

### 2.4. Characterization

X-ray diffraction (XRD) patterns were obtained on X-ray analyzer (D/max-1200) with a Cu target Kα radiation (λ = 0.1541 nm) at a generator voltage of 36 kV and a current of 40 mA. Analyses were performed under a 2θ range of 10.0°–80.0° at a scanning rate of 8°/min. Fourier-transform infrared (FT-IR) spectra were obtained on a Nicolet 6700 spectrometer. UV-vis spectra were recorded by a Hitachi 330 UV-vis spectrophotometer. X-ray photoelectron spectroscopy (XPS) profiles were recorded by an ESCALAB 25 X-ray photoelectron spectrometer (Thermo-VG Scientific). Transmission electron microscope (TEM) images were observed by using Philips TECNAL-10 transmission electron microscope. Scanning electron microscope (SEM) images were performed on JSM-6330F scanning electron microscope with an accelerating voltage of 20.0 kV, the fracture surface of sample was coated with a thin layer of gold before analysis. ESR signals of h<sup>+</sup> in powder, •O<sub>2</sub><sup>-</sup> in water and •OH in



Scheme 1. Schematic illustration of the synthesis process of the 10-CNМ.

methanol with 5, 5-dimethyl-1-pyrroline *N*-oxide (DMPO) were recorded with a Bruker a300 ESR spectrometer.

### 2.5. Photocatalytic degradation experiment

The photocatalytic performances of the as-prepared samples were evaluated by monitoring their abilities to degrade the methyl blue (MB) dyes induced by a 300 W Xenon lamp (Institution of Electric Source, Beijing) with 400 nm cut-off filter. The temperature of the reaction solution was kept at 25°C. In a typical experiment, 50 mg photocatalysts were suspended in organic dye aqueous solution (100 mL, 20 mg/L) under magnetically stirring in the dark for 2 h to reach the adsorption-desorption equilibrium. During the visible light irradiation, 5 mL was taken from each sample at a certain time interval. Subsequently, the solutions were measured by the UV-vis spectrophotometer at 664 nm. The concentration changes were described by  $C/C_0$ , where  $C$  was the remained concentration of dye and  $C_0$  was the initial concentration of dye (after subtraction of the concentration of dye, which was adsorbed to the catalysts). The organic dye degradation percent ( $D_p$ ) was determined by

$$D_p = 1 - \left( \frac{C}{C_0} \right) \times 100\% \quad (1)$$

## 3. Results and discussion

### 3.1. Characterization of CNM

The XRD patterns of  $g\text{-C}_3\text{N}_4$ ,  $\text{MoS}_2$ , and series of CNM were shown in Fig. 1(a). It could be seen that  $g\text{-C}_3\text{N}_4$  exhibited two distinct peaks at 27.6° and 12.93°, which could be indexed as the (110) and (100) diffraction planes of the  $g\text{-C}_3\text{N}_4$  (JCPDS 50-1250) [21–23]. The strong peak at 27.6° related to the in-plane structural packing motif, and the weak peak at 12.93° corresponded to the inter-layer stacking of aromatic systems.

The diffraction peaks of pure  $\text{MoS}_2$  appeared at 14.5, 29.3, 33.0, 34.1, 38.4, 41.1, 44.5, 48.1, 58.3, 60.5, and 76.1, which

corresponded to (003), (006), (101), (012), (104), (015), (009), (107), (110), (113), and (119) diffraction planes, respectively (JCPDS 17-0744). No diffraction peaks from residues or impurities could be observed, indicating the high purity of the hexagonal  $\text{MoS}_2$  product [24]. The result indicated that the pure  $\text{MoS}_2$  had been successfully synthesized via calcination method. Fig. 1(b) showed the X-ray diffraction (XRD) patterns of the CNM prepared with different weight ratios of melamine and  $\text{MoS}_2$ . The diffraction peaks of CNM were corresponding to the diffraction of  $g\text{-C}_3\text{N}_4$  and  $\text{MoS}_2$ , respectively. Therefore, it revealed that  $g\text{-C}_3\text{N}_4$  was successfully coupled with  $\text{MoS}_2$ .

FT-IR spectra of 10-CNM, pure  $g\text{-C}_3\text{N}_4$ , and pure  $\text{MoS}_2$  were showed in Fig. 2. The peaks at 1240, 1320, 1403, and 1640  $\text{cm}^{-1}$  were related to the typical stretching modes of CN heterocycles in  $g\text{-C}_3\text{N}_4$  [25]. The peak at 808  $\text{cm}^{-1}$  was ascribed to the characteristic breathing mode of triazine units and the stretching mode of NH in  $g\text{-C}_3\text{N}_4$  [26].

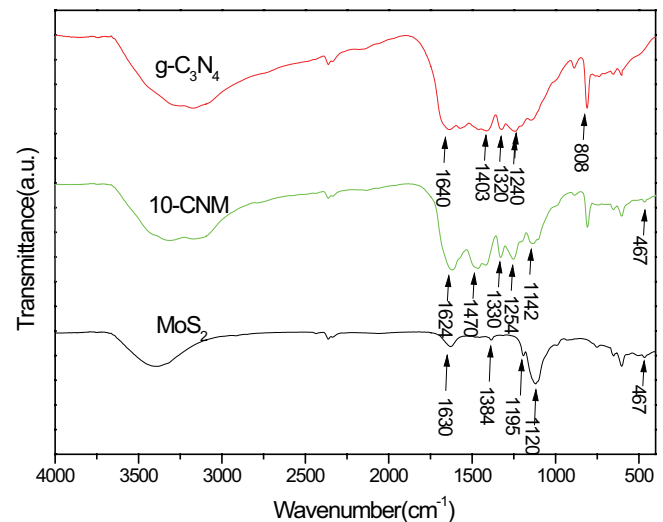


Fig. 2. FT-IR spectra of pure  $\text{MoS}_2$ , pure  $g\text{-C}_3\text{N}_4$  and 10-CNM.

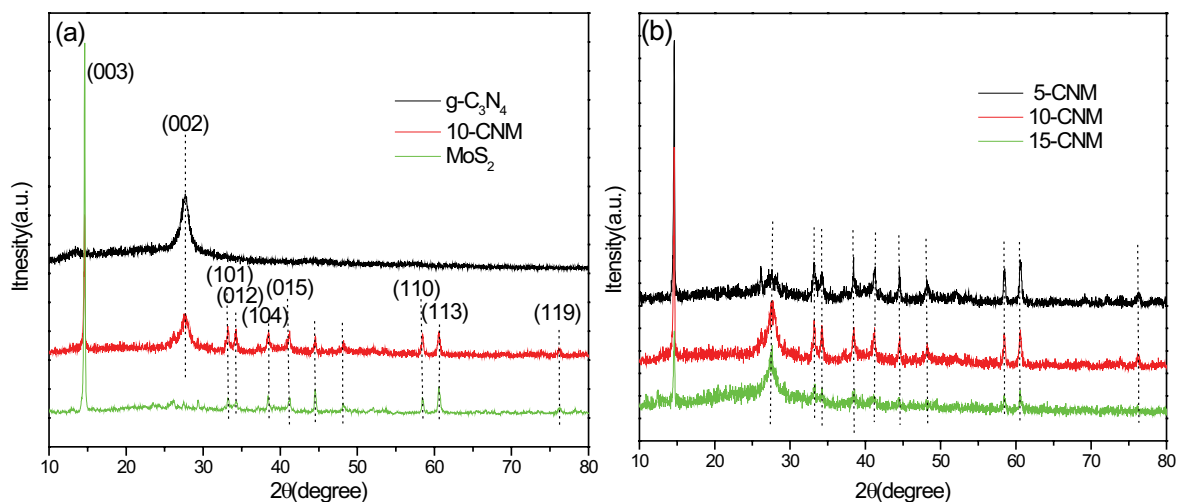


Fig. 1. XRD patterns of pure  $\text{MoS}_2$ , pure  $g\text{-C}_3\text{N}_4$ , and 10-CNM (a) 5-CNM, 10-CNM and 15-CNM (b).

For pure MoS<sub>2</sub>, the peak observed at 467 cm<sup>-1</sup> was ascribed to the Mo–S bond [27]. Moreover, the peaks at 1630, 1384, and 1195 cm<sup>-1</sup> were associated with the characteristic bands of MoS<sub>2</sub>. Particularly, 10-CNM and pure g-C<sub>3</sub>N<sub>4</sub> possessed similar FT-IR spectra, indicating that the introduction of MoS<sub>2</sub> nanosheets did not change the functional groups of g-C<sub>3</sub>N<sub>4</sub>. With the introduction of MoS<sub>2</sub>, the peak at 808 and 1240 cm<sup>-1</sup> of g-C<sub>3</sub>N<sub>4</sub> exhibited a red shift, which might be attributed to the interaction between g-C<sub>3</sub>N<sub>4</sub> and MoS<sub>2</sub> [28].

The morphologies of the pure g-C<sub>3</sub>N<sub>4</sub>, pure MoS<sub>2</sub> and 10-CNM were investigated by SEM (Fig. 3) and TEM (Fig. 4). From the SEM images in Fig. 3(a), the pure g-C<sub>3</sub>N<sub>4</sub> showed

thin sheet-like morphology, while the pure MoS<sub>2</sub> appeared to be plate-like morphology with an average diameter of 50 nm (Fig. 3(b)). Both of the morphology of g-C<sub>3</sub>N<sub>4</sub> and MoS<sub>2</sub> in 10-CNM were retained (Fig. 3(c)). And the plate-like MoS<sub>2</sub> cut through the g-C<sub>3</sub>N<sub>4</sub> sheet like the grass grew out of the ground. The high magnification SEM image (Fig. 3(d)) shows that the thick of MoS<sub>2</sub> plate was about 50 nm.

As shown in Figs. 4(a) and (b), the pure g-C<sub>3</sub>N<sub>4</sub> had thin sheet structures with rolled and bucked edges, while the pure MoS<sub>2</sub> possessed plate morphology. The TEM images of 10-CNM (Figs. 4(c) and (d)) illustrated that the MoS<sub>2</sub> plate and g-C<sub>3</sub>N<sub>4</sub> sheets were combined well. The spacing of the lattice

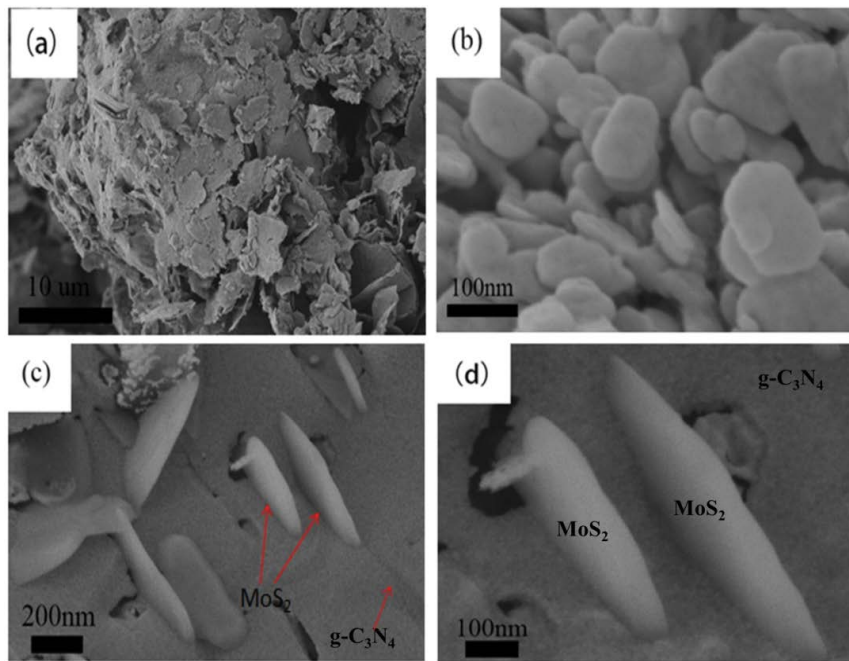


Fig. 3. The SEM images of pure g-C<sub>3</sub>N<sub>4</sub> (a), pure MoS<sub>2</sub> (b), and 10-CNM (c and d).

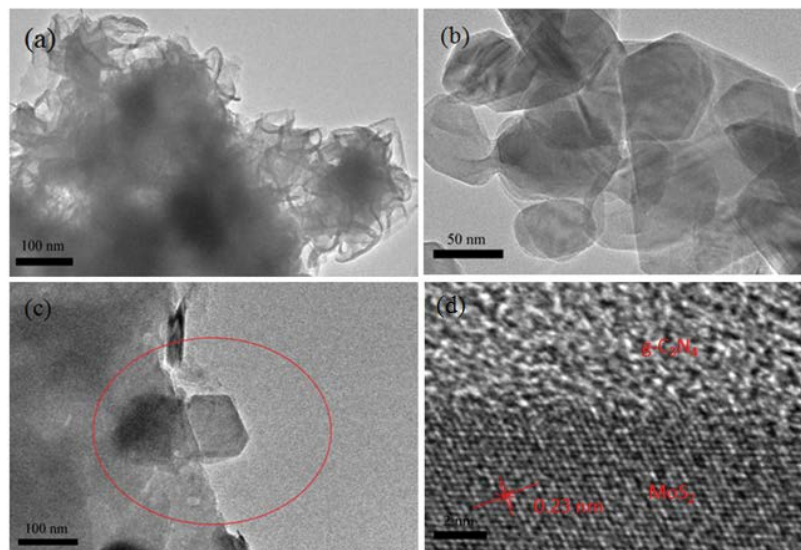


Fig. 4. HRTEM images of pure g-C<sub>3</sub>N<sub>4</sub> (a), pure MoS<sub>2</sub> (b), 10-CNM (c and d).

fringes (the HRTEM image) was about 0.23 nm, corresponding to the (104) plane of  $\text{MoS}_2$  (JCPDS No. 17-0744). HRTEM analysis gave direct evidence for the heterojunction between  $\text{MoS}_2$  and  $\text{g-C}_3\text{N}_4$ , which might improve the separation of electron holes during the photocatalytic process [29].

The chemical components and the states of C, N, Mo and S in 10-CNMs were investigated by the XPS. Fig. 5(a) indicates the presence of C, N, Mo, and S in the composite. In Fig. 5(b), the XPS peaks of C 1s were observed at 284.9 and 288.4 eV, corresponding to  $sp^2$  C–C bonds and  $sp^2$ -bonded carbon (N–C=N) in the triazine rings of  $\text{g-C}_3\text{N}_4$  [30]. As observed in Fig. 5(c), there were three peaks at about 398.6, 399.8, and 401.0 eV in the N 1s spectrum, which could be ascribed to C–N–C, N–(C)<sub>3</sub>, and N–H, respectively [31]. And the peaks of Mo 3d in Fig. 5(d) are fitted into two peaks at 229.2 ( $3d_{5/2}$ ) and 232.5 eV ( $3d_{3/2}$ ), suggesting that Mo element in CNM mainly

existed in the form of  $\text{Mo}^{4+}$ . In Fig. 5(e), the main S 2p peak at a binding energy of 161.9 eV could be attributed to the crystal lattice of  $\text{S}^{2-}$  [32]. The aforementioned observations indicated that  $\text{MoS}_2$  was incorporated with  $\text{g-C}_3\text{N}_4$  successfully.

### 3.2. Optical properties

As shown in Figs. 6(a) and 6(b), the pure  $\text{g-C}_3\text{N}_4$  exhibited an absorption edge at 450 nm corresponded to the band gap of 2.73 eV, and the pure  $\text{MoS}_2$  had an adsorption edge at 690 nm corresponded to the band gap of 1.83 eV. For  $\text{g-C}_3\text{N}_4/\text{MoS}_2$  heterojunction (Fig. 6(c)), the visible light absorption of the composite dramatically increased when the weight ratio of  $\text{g-C}_3\text{N}_4$  and  $\text{MoS}_2$  increased, which might be attributed to the weaker visible light absorption of  $\text{g-C}_3\text{N}_4$  compared to that of  $\text{MoS}_2$ . Fig. 6(d) showed the PL spectra of as-prepared samples

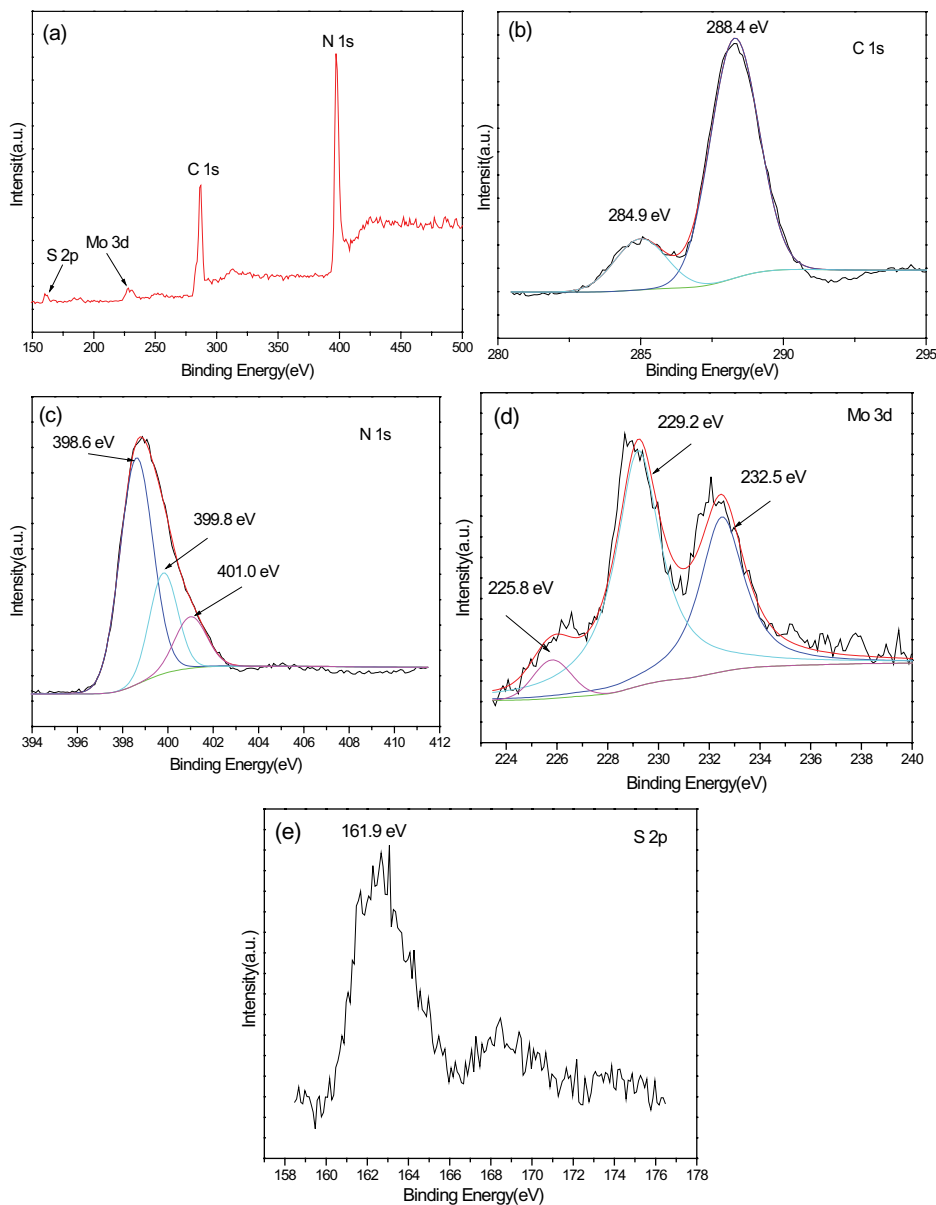


Fig. 5. The XPS spectra of the 10-CNMs: survey (a), C 1s (b), N 1s (c), Mo 3d (d), and S 2p (e).

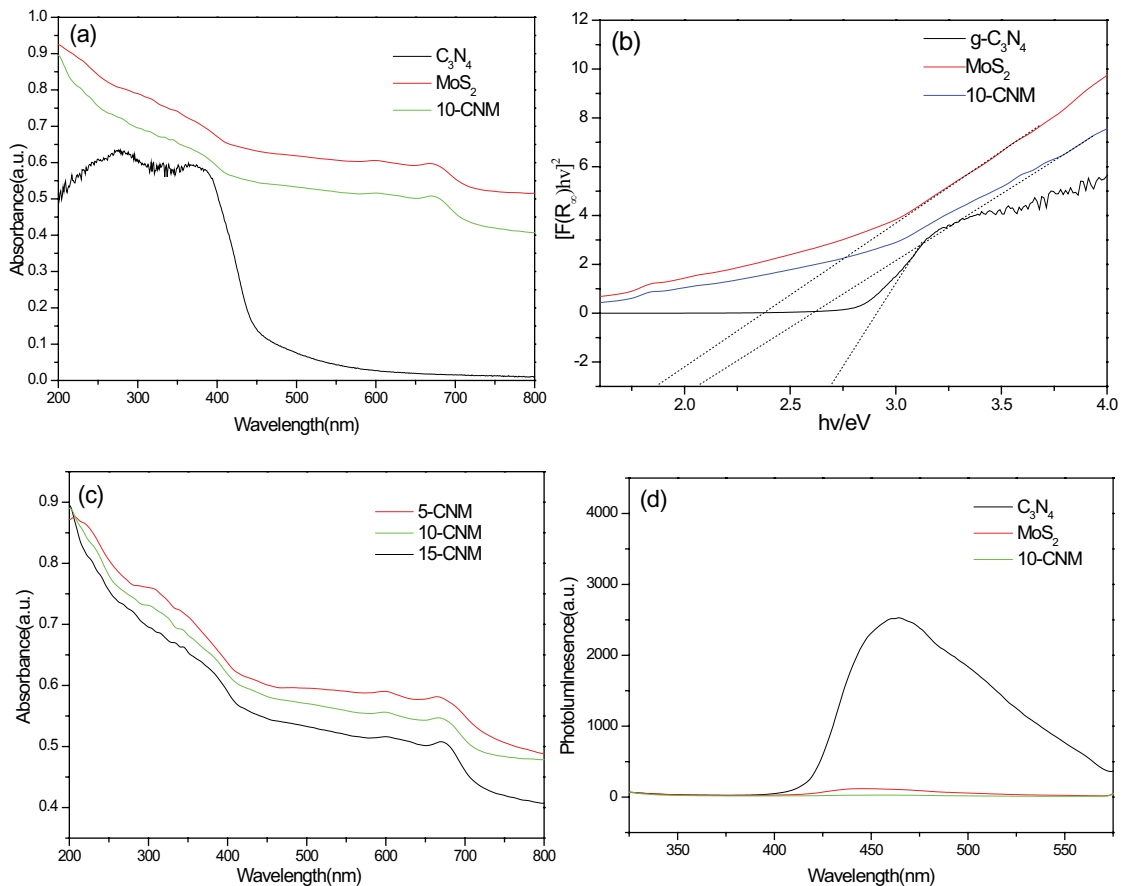


Fig. 6. UV-vis diffuse reflectance spectra (a–c), and photoluminescence emission spectra (d) of pure  $g\text{-C}_3\text{N}_4$ , pure  $\text{MoS}_2$ , and 10-CNM.

under the excitation wavelength of 325 nm. Pure  $g\text{-C}_3\text{N}_4$  showed an emission peak at about 455 nm, corresponding to the band gap for the recombination of photogenerated electrons and holes [33]. The PL emission of  $\text{MoS}_2$  was rather low because the  $\text{MoS}_2$  powder was black. Significantly, the PL emission of 10-CNM was far lower than that of pure  $g\text{-C}_3\text{N}_4$ , revealing that the charge recombination was further reduced. In general, the recombination of photogenerated electron-hole pairs could release energy to form the PL emission, and the lower PL intensity indicated the lower recombination of photogenerated charge carrier, which led to higher photocatalytic activity [34]. Obviously, the PL emission intensity of  $g\text{-C}_3\text{N}_4$  decreased after the loading of  $\text{MoS}_2$ , suggesting that the charge recombination could be efficiently prevented by  $\text{MoS}_2$  modification.

### 3.3. Photocatalytic activity and mechanisms

The photocatalytic activity of as-synthesized CNM was evaluated by MB (20, 100 mL) degradation under visible light irradiation. The dye aqueous solution was very stable, and almost no decomposition was observed in the absence of catalyst. Fig. 7(a) shows the absorption and the photodegradation of the samples toward MB under dark and visible light irradiation. A total of 10% of MB was adsorbed in 10-CNM, while over 20% and 15% of MB were adsorbed in  $\text{MoS}_2$  and  $g\text{-C}_3\text{N}_4$ . Because the adsorption activity sites

in  $g\text{-C}_3\text{N}_4$  were occupied by  $\text{MoS}_2$  plate, the adsorption capability of 10-CNM was decreased. Although exhibited lower adsorption toward contaminants, CNM exhibited excellent photocatalytic activity. Under the visible light irradiation, CNM exhibited much higher degradation rate compared with pure  $\text{MoS}_2$  and  $g\text{-C}_3\text{N}_4$ . The highest activity was obtained over 10-CNM, resulting in 94% degradation for MB within 120 min visible light irradiation. The pseudo-first-order kinetic model could be adopted following the equation:

$$\ln\left(\frac{C}{C_0}\right) = -kt \quad (2)$$

The reaction rate constants of 5-CNM, 10-CNM, and 15-CNM displayed in Fig. 7(b) were calculated to be 0.03466, 0.07732, and 0.03698  $\text{min}^{-1}$ , respectively.

In order to further understand the mineralization properties of photocatalysts, the TOC in MB photodegradation of different photocatalysts after 2 h was determined. As shown in Fig. 7(c), it was clearly observed that maximum photodegradation (93.7%) and TOC removal (76.2%) were achieved using 10-CNM. Hence, most of the dye molecules were mineralized during photodegradation process. As shown in Fig. 7(d), 10-CNM exhibited inappreciable loss of photocatalytic activity after four-cycle reaction processes, revealing the excellent stability of this kind of ternary photocatalyst.

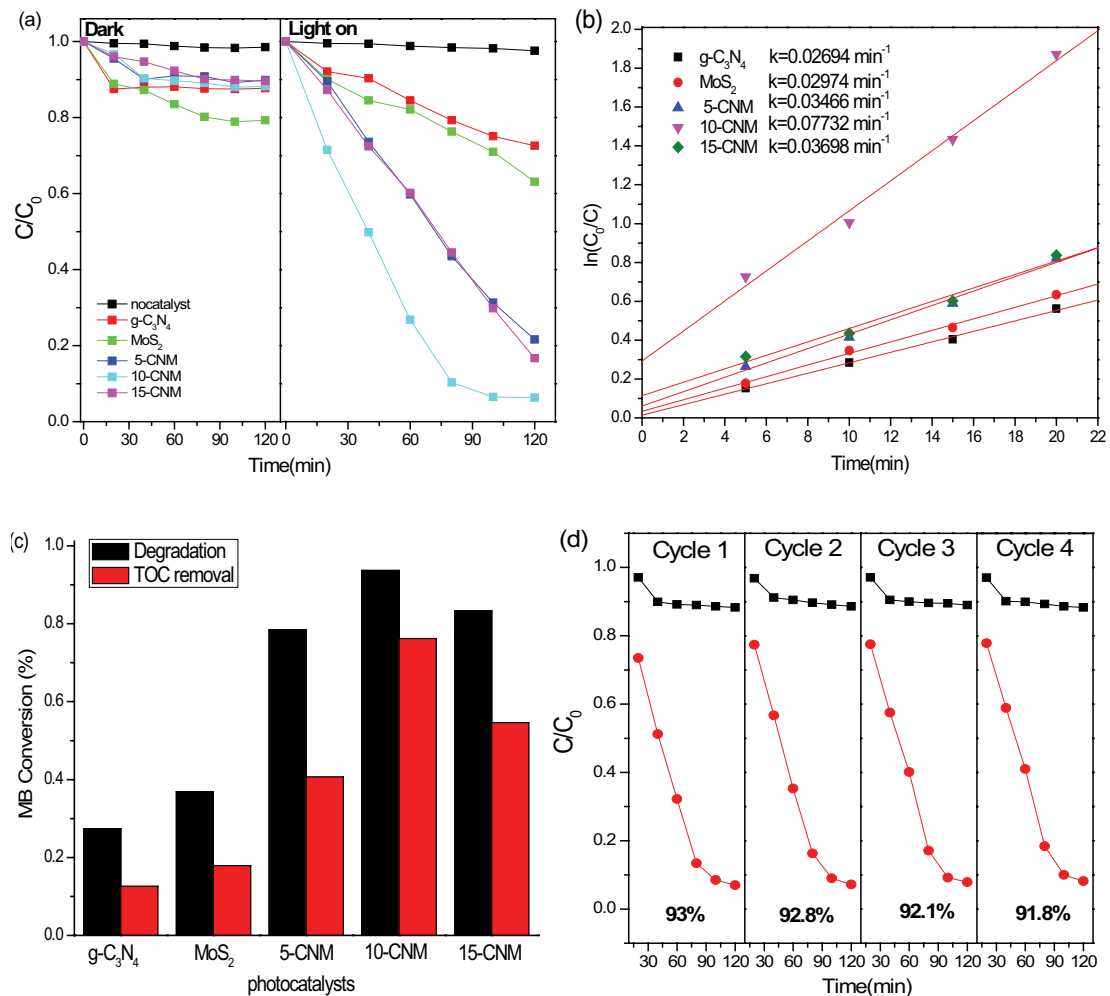


Fig. 7. Comparison of the absorption of MB under dark and photocatalytic activity of MB under visible light irradiation over different samples (a), Kinetic plots for MB using different samples after 20 min of visible light irradiation (b), Comparison of photo-degradation and TOC removal percentage of MB in the presence of different samples (c), Cycle runs of 10-CNM for MB removal (d).

To determine the main active species in this photocatalytic process, the ESR spin-trap with DMPO technique was carried out. As shown in Figs. 8(a) and (b), when the samples were exposed to visible light, the typical signals of  $\bullet\text{O}_2^-$  and  $\bullet\text{OH}$  were detected in water and in methanol solution, respectively, while no signal could be observed in dark. The ERS signal of DMPO- $\bullet\text{O}_2^-$  had four characteristic peaks, which revealed the photo-generated electrons in the CB of semiconductors could be converted into  $\bullet\text{O}_2^-$  radicals during the photo degradation system. Compared with DMPO- $\bullet\text{O}_2^-$ , the signal of DMPO- $\bullet\text{OH}$  was much weaker under visible light. This result indicated that  $\bullet\text{OH}$  played a partial role during the photocatalytic process and  $\text{O}_2^{\bullet-}$  was the main photocatalytic active groups. Additionally, the peak intensity of the  $\text{h}^+$  under light illumination was much stronger than that in the dark (Fig. 8(c)), revealing that  $\text{h}^+$  also played a vital role in the enhanced photocatalytic performance.

The possible mechanism for photocatalytic degradation of CNM photocatalysts was proposed and presented in Scheme 2. The VB and CB can be calculated according to the empirical equation [35]:

$$E_{\text{CB}} = X - E^e - 0.5E_g \quad (3)$$

$$E_{\text{VB}} = E_{\text{CB}} + E_g \quad (4)$$

The  $X$  values for g-C<sub>3</sub>N<sub>4</sub> and MoS<sub>2</sub> are 4.73 and 5.33 eV, respectively [36,37].  $E^e$  is the energy of free electrons on the hydrogen scale (about 4.5 eV), and  $E_g$  is the band gap energy of the semiconductor ( $E_g$  for g-C<sub>3</sub>N<sub>4</sub> and MoS<sub>2</sub> are 2.73 and 1.83 eV, respectively). From the calculation, it is known that the  $E_{\text{CB}}$  of g-C<sub>3</sub>N<sub>4</sub> and MoS<sub>2</sub> are about -1.13 and -0.08 eV, respectively. The  $E_{\text{VB}}$  of g-C<sub>3</sub>N<sub>4</sub> and MoS<sub>2</sub> are estimated to be 1.4 and 1.75 eV, respectively. It is well established that an efficient separation of photoinduced electrons and holes is of great importance for improving the photocatalytic activity. There was a match of energy bands between g-C<sub>3</sub>N<sub>4</sub> and MoS<sub>2</sub> to form g-C<sub>3</sub>N<sub>4</sub>/MoS<sub>2</sub> heterojunction. Both g-C<sub>3</sub>N<sub>4</sub> and MoS<sub>2</sub> were excited to generate electrons and holes under the visible light irradiation. For the CB potential of the g-C<sub>3</sub>N<sub>4</sub> was more negative than that of the MoS<sub>2</sub>, the photoinduced electrons in the CB of the g-C<sub>3</sub>N<sub>4</sub> could easily transfer to that

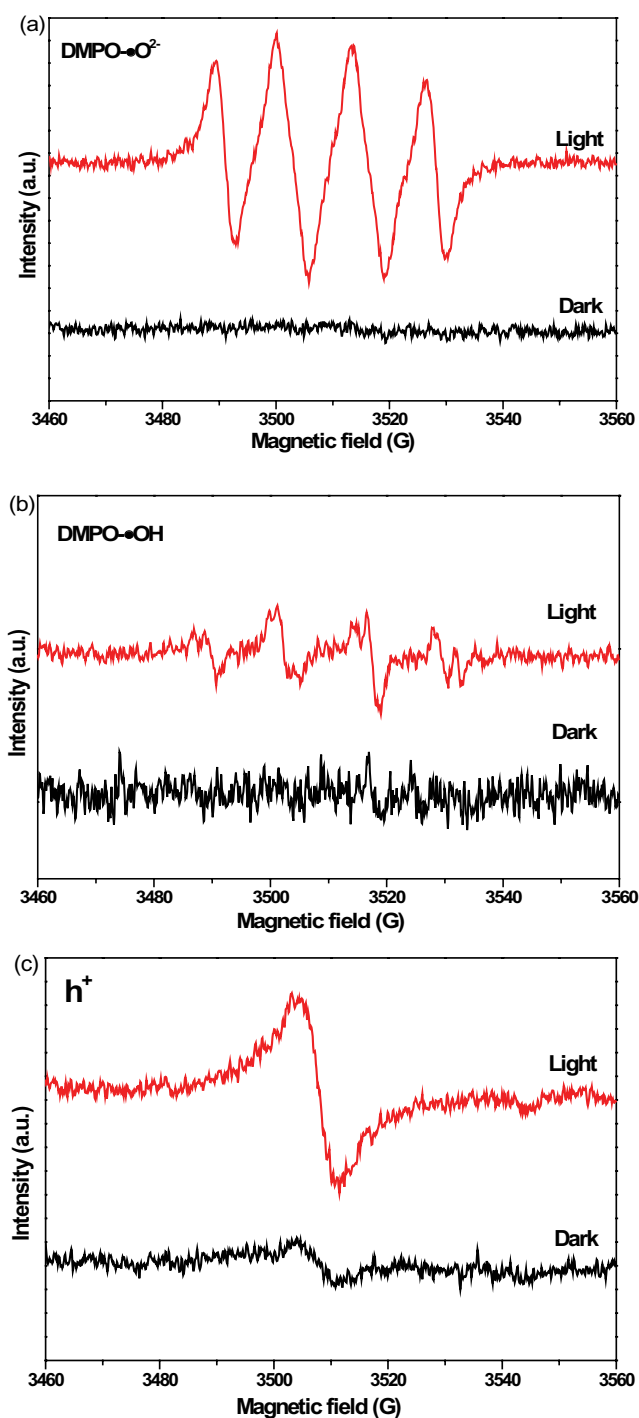
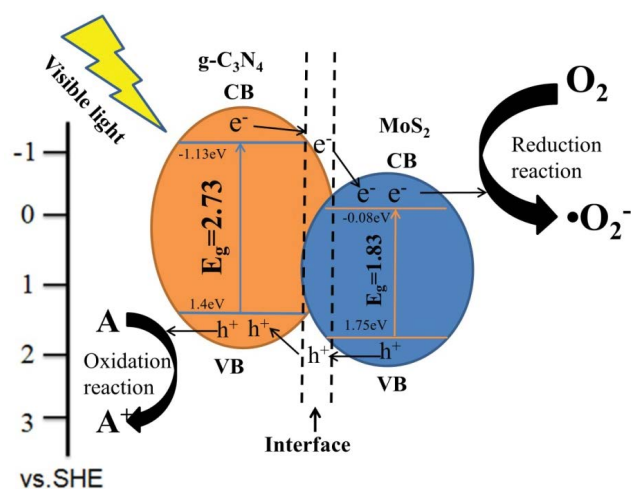


Fig. 8. ESR spectra of 10-CNM before and after visible light irradiation: (a) DMPO- $\bullet\text{O}_2^-$  in methanol dispersion, (b) DMPO- $\bullet\text{OH}$  in aqueous dispersion and (c)  $\text{h}^+$  in powder.

of the  $\text{MoS}_2$  through the intimate interface. Similarly, the holes in the VB of  $\text{MoS}_2$  could move to that of the  $\text{g-C}_3\text{N}_4$ . As a result, the excellent heterostructure between  $\text{g-C}_3\text{N}_4$  and  $\text{MoS}_2$  could achieve the effectively promoted separation of photogenerated electron-hole pairs and enhanced the photocatalytic degradation performance. Therefore, the formation



Scheme 2. Schematic illustration of the mechanism of enhanced photocatalytic activity of 10-CNM.

of the heterojunction could be considered as the primary factor for the enhanced photocatalytic activity.

#### 4. Conclusion

In summary,  $\text{g-C}_3\text{N}_4/\text{MoS}_2$  heterojunction has been successfully synthesized by a facile calcination method. Experimental results have confirmed that the as-prepared CNM composite exhibited enhanced photocatalytic activity. The highest photocatalytic activity is observed for the 10-CNM sample, the corresponding degradation rate for MB is 94% after being irradiated for 2 h under visible light. The enhanced photocatalytic can be ascribed to the heterostructure formed between  $\text{g-C}_3\text{N}_4$  and  $\text{MoS}_2$ , which can accelerate the transfer and separation of photoelectron. It is believed that this stable, efficient, and easy-made photocatalyst is promising as a new candidate for widespread applications.

#### Acknowledgments

This work was supported by the Department of Science and Technology of Guangdong Province (2016A010103047).

#### References

- [1] X.B. Chen, S.H. Shen, L.J. Guo, S.S. Mao, Semiconductor-based photocatalytic hydrogen generation, *Chem. Rev.*, 110 (2010) 6503–6570.
- [2] M.R. Hoffmann, S.T. Martin, W. Choi, D.W. Bahnemann, Environmental applications of semiconductor photocatalysis, *Chem. Rev.*, 95 (1995) 69–96.
- [3] S.K. Li, F.Z. Huang, Y. Wang, Y.H. Shen, L.G. Qiu, A.J. Xie, S.J. Xu, Magnetic  $\text{Fe}_3\text{O}_4@\text{C}/\text{Cu}_2\text{O}$  composites with bean-like core/shell nanostructures: synthesis, properties and application in recyclable photocatalytic degradation of dye pollutants, *J. Mater. Chem.*, 21 (2011) 7459–7466.
- [4] X. Wang, K. Maeda, A. Thomas, K. Takane, G. Xin, J.M. Carlsson, K. Domen, M. Antonietti, A metal-free polymeric photocatalyst for hydrogen production from water under visible light, *Nat. Mater.*, 8 (2009) 76–80.
- [5] S.C. Yan, Z.S. Li, Z.G. Zou, Photodegradation performance of  $\text{g-C}_3\text{N}_4$  fabricated by directly heating melamine, *Langmuir*, 25 (2009) 10397–10401.

- [6] Q. Xiang, J. Yu, M. Jaroniec, Preparation and enhanced visible-light photocatalytic H<sub>2</sub>-production activity of graphene/g-C<sub>3</sub>N<sub>4</sub> composites, *J. Phys. Chem. C*, 115 (2011) 7355–7363.
- [7] M. Groenewolt, M. Antonietti, Synthesis of g-C<sub>3</sub>N<sub>4</sub> nanoparticles in mesoporous silica host matrices, *Adv. Mater.*, 17 (2005) 1789–1792.
- [8] W. Cui, J.Y. Li, F. Dong, Y.J. Sun, G.M. Jiang, W.L. Cen, S.C. Lee, Z.B. Wu, Highly efficient performance and conversion pathway of photocatalytic NO oxidation on SrO-clusters@amorphous carbon nitride, *Environ. Sci. Technol.*, 51 (2017) 10682–10690.
- [9] A. Thomas, A. Fischer, F. Goettmann, M. Antonietti, J.O. Müller, R. Schlögl, J.M. Carlsson, Graphitic carbon nitride materials: variation of structure and morphology and their use as metal-free catalysts, *J. Mater. Chem.*, 18 (2008) 4893–4908.
- [10] J. Zhang, M. Zhang, R.Q. Sun, X.C. Wang, A facile band alignment of polymeric carbon nitride semiconductors to construct isotype heterojunctions, *Angew. Chem.*, 124 (2012) 10292–10296.
- [11] Y. Zhang, J. Liu, G. Wu, W. Chen, Porous graphitic carbon nitride synthesized via direct polymerization of urea for efficient sunlight-driven photocatalytic hydrogen production, *Nanoscale*, 4 (2012) 5300–5303.
- [12] W. Cui, J.Y. Li, W.L. Cen, Y.J. Sun, S.C. Lee, F. Dong, Steering the interlayer energy barrier and charge flow via bioriented transportation channels in g-C<sub>3</sub>N<sub>4</sub>: enhanced photocatalysis and reaction mechanism, *J. Catal.*, 352 (2017) 351–360.
- [13] G.M. Jiang, X.W. Li, M.N. Lan, T. Shen, X.S. Lv, F. Dong, S. Zhang, Monodisperse bismuth nanoparticles decorated graphitic carbon nitride: enhanced visible-light-response photocatalytic NO removal and reaction pathway, *Appl. Catal. B: Environ.*, 205 (2017) 532–540.
- [14] X.Y. Li, Y.H. Pi, L.Q. Wu, Z. Lin, J. Xiao, Facilitation of the visible light-induced Fenton-like excitation of H<sub>2</sub>O<sub>2</sub> via heterojunction of g-C<sub>3</sub>N<sub>4</sub>/NH<sub>2</sub>-iron terephthalate metal-organic framework for MB degradation, *Appl. Catal. B: Environ.*, 202 (2017) 653–663.
- [15] S.W. Cao, Y.P. Yuan, J. Fang, M.M. Shahjamali, F.Y.C. Boey, J. Barber, S.C.J. Loo, C. Xue, In-situ growth of CdS quantum dots on g-C<sub>3</sub>N<sub>4</sub> nanosheets for highly efficient photocatalytic hydrogen generation under visible light irradiation, *Int. J. Hydrogen Energy*, 38 (2013) 1258–1266.
- [16] W. Liu, M.L. Wang, C.X. Xu, S.F. Chen, Facile synthesis of g-C<sub>3</sub>N<sub>4</sub>/ZnO composite with enhanced visible light photo-oxidation and photoreduction properties, *Chem. Eng. J.*, 209 (2012) 386–393.
- [17] L. Ge, C.C. Han, J. Liu, Novel visible light-induced g-C<sub>3</sub>N<sub>4</sub>/Bi<sub>2</sub>WO<sub>6</sub> composite photocatalysts for efficient degradation of methyl orange, *Appl. Catal. B: Environ.*, 108 (2011) 100–107.
- [18] X. Zhang, Z. Lai, C. Tan, H. Zhang, Solution-processed two-dimensional MoS<sub>2</sub> nanosheets: preparation, hybridization, and applications, *Angew. Chem. Int. Edit.*, 55 (2016) 8816–8838.
- [19] K.F. Mak, C. Lee, J. Hone, J. Shan, T.F. Heinz, Atomically thin MoS<sub>2</sub>: a new direct-gap semiconductor, *Phys. Rev. Lett.*, 105 (2010) 136805.
- [20] Y. Zhang, X. Bo, A. Nsabimana, C. Luhana, G. Wang, H. Wang, M. Li, L.P. Guo, Fabrication of 2D ordered mesoporous carbon nitride and its use as electrochemical sensing platform for H<sub>2</sub>O<sub>2</sub>, nitrobenzene, and NADH detection, *Biosens. Bioelectron.*, 53 (2014) 250–256.
- [21] W.K. Jo, T. Adinaveen, J.J. Vijaya, N.C.S. Selvam, Synthesis of MoS<sub>2</sub> nanosheet supported Z-scheme TiO<sub>2</sub>/g-C<sub>3</sub>N<sub>4</sub> photocatalysts for the enhanced photocatalytic degradation of organic water pollutants, *RSC Adv.*, 26 (2016) 10487–10497.
- [22] G. Liao, S. Chen, X. Quan, H.T. Yu, H.M. Zhao, Graphene oxide modified g-C<sub>3</sub>N<sub>4</sub> hybrid with enhanced photocatalytic capability under visible light irradiation, *J. Mater. Chem.*, 22 (2012) 2721–2726.
- [23] P. Chen, T.Y. Xiao, Y.H. Qian, S.S. Li, S.H. Yu, A nitrogen-doped graphene/carbon nanotube nanocomposite with synergistically enhanced electrochemical activity, *Adv. Mater.*, 25 (2013) 3192–3196.
- [24] S. Ma, J. Xie, J.Q. Wen, K.L. He, X. Li, W. Liu, X.C. Zhang, Constructing 2D layered hybrid CdS nanosheets/MoS<sub>2</sub> heterojunctions for enhanced visible-light photocatalytic H<sub>2</sub> generation, *Appl. Surf. Sci.*, 391 (2017) 580–591.
- [25] X. Li, J. Zhang, L. Shen, Y.M. Ma, W.W. Lei, Q.L. Cui, G.T. Zou, Preparation and characterization of graphitic carbon nitride through pyrolysis of melamine, *Appl. Phys. A: Mater.*, 94 (2013) 387–392.
- [26] F. Dong, Z. Zhao, T. Xiong, Z. Ni, W.D. Zhang, Y.J. Sun, W.K. Ho, In situ construction of g-C<sub>3</sub>N<sub>4</sub>/g-C<sub>3</sub>N<sub>4</sub> metal-free heterojunction for enhanced visible-light photocatalysis, *ACS Appl. Mater. Interfaces*, 5 (2013) 11392–11401.
- [27] S. Liu, X. Zhang, H. Shao, J. Xu, F.Y. Chen, Y. Feng, Preparation of MoS<sub>2</sub> nanofibers by electrospinning, *Mater. Lett.*, 73 (2012) 223–225.
- [28] Y. Hou, Z. Wen, S. Cui, X. Guo, J. Chen, Constructing 2D porous graphitic C<sub>3</sub>N<sub>4</sub> nanosheets/nitrogen-doped graphene/layered MoS<sub>2</sub> ternary nanojunction with enhanced photoelectrochemical activity, *Adv. Mater.*, 25 (2013) 6291–6297.
- [29] J. Low, S. Cao, J. Yu, S. Wageh, Two-dimensional layered composite photocatalysts, *Chem. Commun.*, 50 (2014) 10768–10777.
- [30] J. Li, E.Z. Liu, Y.N. Ma, X.Y. Hu, J. Wan, L. Sun, J. Fan, Synthesis of MoS<sub>2</sub>/g-C<sub>3</sub>N<sub>4</sub> nanosheets as 2D heterojunction photocatalysts with enhanced visible light activity, *Appl. Surf. Sci.*, 364 (2016) 694–702.
- [31] X. Yang, Z. Chen, J. Xu, H. Tang, K.M. Chen, Y. Jiang, Tuning the morphology of g-C<sub>3</sub>N<sub>4</sub> for improvement of Z-scheme photocatalytic water oxidation, *ACS Appl. Mater. Interfaces*, 7 (2015) 15285–15293.
- [32] C. Altavilla, M. Sarno, P. Ciambelli, A novel wet chemistry approach for the synthesis of hybrid 2D free-floating single or multilayer nanosheets of MS<sub>2</sub>@oleylamine (M=Mo, W), *Chem. Mater.*, 23 (2011) 3879–3885.
- [33] P. Gomathisankar, K. Hachisuka, H. Katsumata, T. Suzuki, K. Funasaka, S. Kaneco, Photocatalytic hydrogen production from aqueous Na<sub>2</sub>S<sup>+</sup> Na<sub>2</sub>SO<sub>3</sub> solution with B-doped ZnO, *ACS Sustain. Chem. Eng.*, 1 (2013) 982–988.
- [34] Q.Y. Lin, L. Li, S.J. Liang, M.H. Liu, J.H. Bi, L. Wu, Efficient synthesis of monolayer carbon nitride 2D nanosheet with tunable concentration and enhanced visible-light photocatalytic activities, *Appl. Catal. B: Environ.*, 163 (2015) 135–142.
- [35] Y.Z. Hong, Y.H. Jiang, C.S. Li, W.Q. Fan, X. Yan, M. Yan, W.D. Shi, In-situ synthesis of direct solid-state Z-scheme V<sub>2</sub>O<sub>5</sub>/g-C<sub>3</sub>N<sub>4</sub> heterojunctions with enhanced visible light efficiency in photocatalytic degradation of pollutants, *Appl. Catal. B: Environ.*, 180 (2016) 663–673.
- [36] J.F. Zhang, Y.F. Hu, X.L. Jiang, S.F. Chen, S.G. Meng, X.L. Fu, Design of a direct Z-scheme photocatalyst: preparation and characterization of Bi<sub>2</sub>O<sub>3</sub>/g-C<sub>3</sub>N<sub>4</sub> with high visible light activity, *J. Hazard. Mater.*, 208 (2014) 713–722.
- [37] B. Weng, X. Zhang, N. Zhang, Z. Tang, Y. Xu, Two-dimensional MoS<sub>2</sub> nanosheet-coated Bi<sub>2</sub>S<sub>3</sub> discoids: synthesis, formation mechanism, and photocatalytic application, *Langmuir*, 31 (2015) 4314–4322.